

Effect of Inflow Turbulence on Premixed Combustion in a Cavity Flameholder

Gabriel B. Goodwin, Ryan F. Johnson, David A. Kessler, Andrew D. Kercher

Naval Research Laboratory
4555 Overlook Ave. SW, Washington, DC, USA 20375
Corresponding author: gabe.goodwin@nrl.navy.mil

Harsha K. Chelliah

Department of Aerospace Engineering
University of Virginia, Charlottesville, VA

Abstract

A discontinuous Galerkin computational fluid dynamics code was used to perform highly resolved simulations of ramjet-mode combustion in the University of Virginia Supersonic Combustion Facility cavity flameholder at a flight enthalpy of Mach 5. The primary goal of the work is to enhance our understanding of the effects of turbulence on fully premixed ramjet combustion with a hydrocarbon fuel. Prior experiments measured a freestream turbulence intensity at the inflow to the cavity ranging from 10 – 15%. A synthetic turbulence inflow generator was implemented for the simulations in this work to reproduce the turbulence at the inflow to the cavity. This reduced computational expense, as the turbulent, non-reacting flow upstream of the cavity was generated by a boundary condition rather than requiring the modeling of the entire upstream domain. Velocity perturbations and turbulence intensity generated by the turbulent inflow boundary condition are shown to match those values measured in the facility using particle induced velocimetry. Simulations were performed both with and without inflow turbulence to study the effect of turbulence on flame stability and structure. In both cases, a cavity-stabilized flame was achieved. The inflow turbulence promoted more robust combustion, causing the flame to propagate further from the cavity into the core flow, broadening the flame angle with respect to the axial flow direction. The flame angle captured in the simulation agrees with experimental results and theoretical prediction. The effect of spatial resolution on the simulations is discussed through a comparison of cases using second-order and third-order accurate discontinuous Galerkin finite elements.

Keywords: Dual-mode scramjet; Turbulent combustion; Numerical simulations; Hypersonics; GPU computing

1 Introduction

Maintaining flame stability in hydrocarbon-fueled dual-mode scramjet engines operating at flight Mach numbers of 4–6 is a significant challenge, as residence time in the combustor approaches the ignition delay of the fuel-air mixture. A common method for promoting flame stability is to introduce regions of recirculation within the combustor using a cavity flameholder. The shear layer that forms at the leading edge of the cavity results in recirculation of the fuel-air mixture within the cavity, increasing residence time and enhancing combustion completeness [1].

Cavity flameholders were found to be successful at stabilizing hydrocarbon flames in supersonic flows, with the stability limits heavily dependent on air inflow conditions, fuel type and injection scheme, and cavity geometry [2]. Subsequent experimental work investigated flame stability in cavity flameholders in both ramjet and scramjet modes, observing flame stabilization location to vary with enthalpy of the airflow in both hydrogen and hydrogen/ethylene fuel mixtures [3]. The dynamics governing the location of the flame within the flameholder and spread into the core flow were explored experimentally and numerically [4]. The authors stated that the spread of combustion from the cavity shear layer into the core flow above the cavity was dominated by the traditional diffusion process as well as the convection process associated with the recirculation flows within the cavity, with a strong coupling between the two processes. Axisymmetric cavity flameholders have recently been used to characterize flame stability limits without the interference of corner boundary layer effects found in planar configurations [5].

The dual-mode, direct-connect scramjet cavity combustor at the University of Virginia Supersonic Combustion Facility (UVASCF), described in detail in [6–8], is used to study combustion of hydrocarbon fuels at flight enthalpies up to Mach 5 with a stagnation temperature of 1200 K. In the facility configuration studied in this work, ethylene is injected far upstream of the cavity flameholder such that the flow into the combustor is a relatively homogeneous mixture of ethylene and air. The UVASCF scramjet combustor is capable of operating with a stable, cavity anchored flame in premixed fuel-air mode for long durations with highly repeatable results [7]. Early experimental work in the facility focused on understanding the mean heat release characteristics and dynamic flame behavior [8, 9]. Fluctuations in heat release were observed to occur primarily in the shear layer between the combustion products in the cavity and the incoming freestream flow of reactants. Recent experiments using planar laser-induced fluorescence (PLIF) have provided detailed measurements and visualizations of ramjet-mode combustion in the UVASCF combustor using an additively manufactured cavity flameholder insert with active cooling of the cavity insert walls [10]. Prior experimental configurations at UVASCF used a cavity embedded in the facility wall, similar to

that used in earlier cavity flame stabilization research [2].

Hybrid Reynolds-Averaged Navier Stokes/Large Eddy Simulations (RANS/LES) of combustion in the UVASCF cavity with fuel injection immediately upstream of embedded-wall cavity found flame angles captured in the simulation to agree with those predicted by classical premixed turbulent flame speed estimates [6, 11]. More recent hybrid RANS/LES computations simulated combustion in the facility in the cavity insert configuration with fuel injection far upstream of the cavity [12]. The simulation results agreed with the aforementioned experimental results using this configuration, available in [10], and provided detailed local flow conditions at the inflow to the cavity flameholder insert. Using this data, boundary conditions were defined for the inflow to the cavity flameholder insert computational domain shown in Fig. 1, which is used for the simulations discussed in this work.

This paper presents the results of highly resolved numerical simulations of the turbulent combustion in the cavity flameholder operating in ramjet mode. The purpose of the current work is to reproduce experimental results and characterize the effect of turbulence in the incoming flow on flame stability and propagation of the flame into the core flow downstream of the cavity. Reducing computational expense by simulating only the cavity flameholder region was desirable for these simulations, which focus on resolving the fine-scale flame dynamics in the combustor rather than the macroscopic dynamics of the entire facility as was done in previous work [12]. A synthetic turbulence generator was used to reproduce the turbulent flow conditions at the inflow to the cavity, as reported in prior simulations and experiments, and simulations were performed both with and without inflow turbulence. JENRE[®], the Naval Research Laboratory's discontinuous Galerkin computational fluid dynamics (DG CFD) code, was used to perform the simulations on a local desktop machine utilizing four Nvidia Titan V graphical processing units (GPUs).

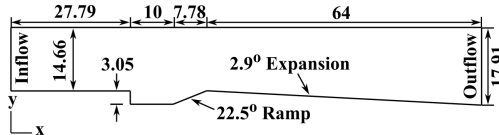


Figure 1: Computational domain with dimensions in mm. Exhaust plenum (radius 1.4 m) not shown.

2 Numerical Method

In this work, we solve the total energy formulation of the reacting Navier Stokes equations [13], given as,

$$\frac{\partial \rho \mathbf{v}}{\partial t} + \nabla \cdot (\rho \mathbf{v} \otimes \mathbf{v} + p \mathbb{I}) = \nabla \cdot \boldsymbol{\tau}, \quad (1)$$

$$\frac{\partial(\rho e_t)}{\partial t} + \nabla \cdot ((\rho e_t + p) \mathbf{v}) = \nabla \cdot \left(\lambda \nabla T - \sum_{i=1}^{N_s} W_i C_i h_i \mathbf{V}_i + \boldsymbol{\tau} \cdot \mathbf{v} \right), \quad (2)$$

$$\frac{\partial C_i}{\partial t} + \nabla \cdot (C_i (\mathbf{v} + \mathbf{V}_i)) = \omega_i \text{ for } i = 1 \dots N_s, \quad (3)$$

where ρ is density, \mathbf{v} is velocity, p is pressure, \mathbb{I} is an identity matrix, $\boldsymbol{\tau}$ is the deviatoric stress tensor as defined in Eq. (2.12) in [13], e_t is total energy, λ is conductivity, T is temperature, N_s is the number of species, W_i is molecular weight, C_i is concentration, h_i is enthalpy, \mathbf{V}_i is diffusion velocity, ω_i is the production source term, and subscript i indicates species i . The production source term is calculated from the progress reaction rates for any number of reactions and reaction types. Pressure is given by the equation of state,

$$p = R^o T \sum_{i=1}^{N_s} C_i, \quad (4)$$

where R^o is the universal gas constant. The species diffusion velocity is given by

$$\mathbf{V}_i = \frac{D_i}{C_i} \nabla C_i - \frac{D_i}{\rho} \nabla \rho, \quad (5)$$

where D_i is the mass-averaged diffusion coefficient. All transport coefficients are calculated using mixture-averaged approaches [14–16]. No artificial viscosity was used in these simulations.

In this model, the total energy is defined as

$$\rho e_t = \rho u + \frac{1}{2} \rho \mathbf{v} \cdot \mathbf{v}, \quad (6)$$

where u is total energy. Internal energy can be defined as a function of total enthalpy, $\rho u = \rho h_t - p$, where h_t is total enthalpy and $\rho h_t = \sum_{i=1}^{N_s} W_i C_i h_i$, where h_i is a nonlinear function with respect to temperature.

Equations (1–3) are discretized using the DG method. The resulting DG space semi-discretization, Eq. (4.2) of [13], is integrated temporally with a second order strong-stability-preserving Runge-Kutta method [17]. The temporal integration of the source term is separated from the temporal integration of the conservation laws via Strang operator splitting. The resulting system of ordinary differential equations, describing the influence of the source term on the temporal evolution of the state, is integrated using a fourth order singly-diagonally implicit Runge-Kutta method [18]. A 19 species, 35 reaction step elementary skeletal mechanism is used to model the ethylene-air combustion [19].

3 Computational Geometry & Problem Set-Up

The computational domain is shown in Fig. 1. This domain is a two-dimensional cross section through the planar cavity flameholder insert. The plenum into which the combustor outflow exhausts is not shown in Fig. 1; it is 1.4 m in radius with atmospheric pressure fixed at the outflow boundary and remaining variables interpolated from the interior. The computational mesh in the plenum is coarse in order to diffuse reflections from the fixed outflow pressure. In the combustor, the computational mesh resolution ranges from $15 \mu\text{m}$ in the cavity shear layer, flame, and against the walls ($y^+ = 3$) to $110 \mu\text{m}$ in the core flow. Second-order accurate $\text{DG}(p = 1)$ triangular mesh elements were used in the initial set of simulations. Third-order accurate $\text{DG}(p = 2)$ elements were used in a subsequent simulation described in Sec. 4.4. Note: the Kolmogorov length scale in the cavity shear layer is approximately $15 \mu\text{m}$ and the width of the smallest flame structures observed in the experimental facility range from $80 - 100 \mu\text{m}$ [9]. The left boundary is a subsonic inflow of a homogeneous ethylene-air mixture at Mach 0.6, 1.72 atm, and 1125 K, with a fuel equivalence ratio of 0.6. Simulations were performed with both laminar and turbulent inflows. The wall boundary conditions are no-slip and isothermal. The temperature conditions for the isothermal walls are shown in Fig. 2 and were obtained from [12].

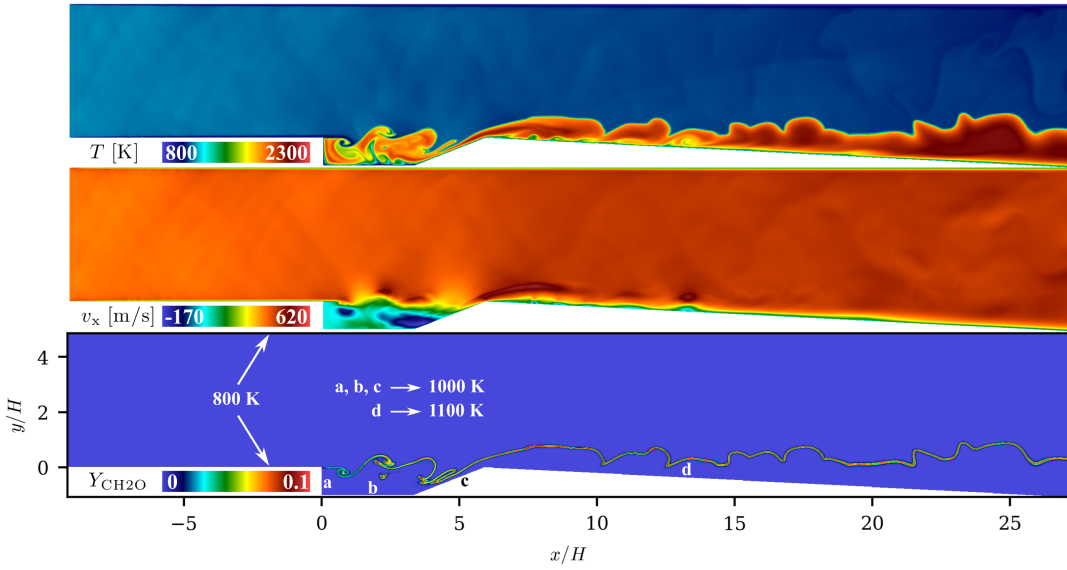


Figure 2: Contours of T , v_x , and $Y_{\text{CH}_2\text{O}}$ show a cavity-stabilized flame with a laminar inflow. Isothermal wall temperatures are shown.

4 Results & Discussion

4.1 Combustion with Laminar Inflow

Figure 2 shows a cavity-stabilized flame with a laminar inflow boundary condition with x and y axes normalized by the cavity height, H , of 3.05 mm. The ethylene-air mixture was ignited after two flow residence times through the combustor by initializing a circular high-temperature region in the cavity. The flame quickly stabilized and anchored to the cavity lip. The T , x -velocity, v_x , and mass fraction of formaldehyde, $Y_{\text{CH}_2\text{O}}$, contours shown in Fig. 2 are sampled two flow residence times following ignition. There is a roll-up of the flame immediately downstream of the cavity lip due to interaction of the flame with the cavity shear layer. In the expanding section, the flame lifts from the lower wall and propagates into the core flow. Two distinct recirculation zones are visible in the v_x plot, with a minimum v_x of -250 m/s at the cavity ramp wall. The peak $Y_{\text{CH}_2\text{O}}$ contour tracks the flame surface, indicating a wrinkled flame front.

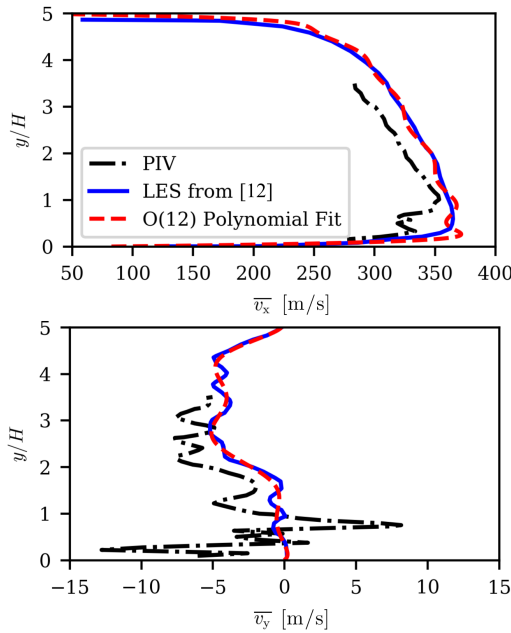


Figure 3: \bar{v}_x and \bar{v}_y profiles across $x/H = -0.05$ used for turbulent inflow.

4.2 Synthetic Turbulence Generation

A synthetic turbulence inflow boundary condition was implemented to generate turbulence at the inflow that reproduces the intensity measured in experiments at UVASCF. The goal in using this boundary condition was to be able to explore the effect of turbulence on the flame, without simulating the entire domain upstream of the cavity flameholder. The boundary condition was implemented using the “Synthetic

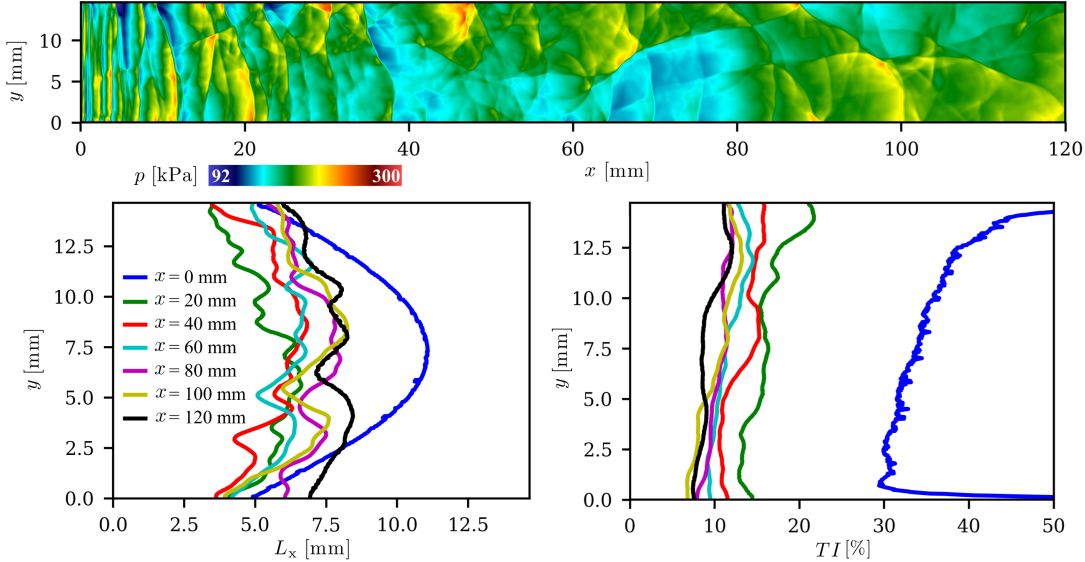


Figure 4: Turbulent inflow into a constant-area channel with L_x and TI plotted across several vertical slices through domain.

Fluctuations” method as detailed in [20]. This method generates isotropic turbulence at a boundary by inducing spatially and temporally correlated velocity perturbations about a user-defined mean velocity, \bar{v} , profile. In the hybrid RANS/LES calculations discussed in [12], the computed \bar{v} profiles are provided at $x/H = -0.05$ and show good agreement with the particle induced velocimetry (PIV) data for the portion of the cavity height where PIV is available. These profiles are shown in Fig. 3. Due to the sizing of the optical window in the combustor at UVASCF, the PIV measurements did not extend to the top wall of the combustor. Twelfth-order polynomials were fit to the LES velocity profiles, as shown in Fig. 3, and taken as the user-defined mean x and y -velocity profiles (\bar{v}_x and \bar{v}_y , respectively) for the turbulent inflow boundary condition.

A simulation was performed to test the turbulent inflow boundary condition and measure turbulence intensity, TI , and turbulent length scale in a constant-area 120 mm long channel, with channel height equal to that of the inlet in the cavity simulations, 14.66 mm. The turbulent inflow was applied at the left boundary, the top and bottom boundaries were slip walls, and the right boundary was a transmissive outflow. Figure 4 shows pressure contours in the domain after two flow residence times as well as TI and turbulent length scale in the streamwise direction, L_x , across several vertical cross sections. Turbulence intensity decays downstream of the boundary condition and approaches an asymptotic value of $\sim 10\%$. Turbulent length scale, calculated using the two-point correlation method outlined in [20], also settles from its forced profile at the inflow boundary to an asymptotic value of ~ 7.5 mm, approximately half the channel height. These results indicate that the turbulent inflow boundary condition generates spatially correlated

turbulence with intensity and length scale that settle to stable values downstream of their forced condition at the inflow boundary.

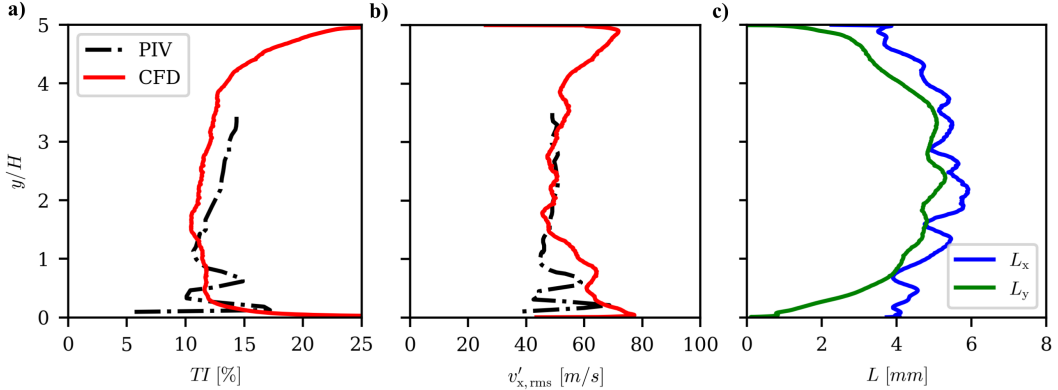


Figure 5: (a) TI (b) $v'_{x,rms}$ (c) L_x and L_y across a vertical slice through the combustor at $x/H = -0.05$.

4.3 Combustion with Turbulent Inflow

The laminar inflow solution shown in Fig. 2 was used as the initial condition for a second simulation in which the synthetic turbulence boundary condition was applied to the cavity inflow. The prescribed conditions for the turbulent inflow were the same as were used in the constant-area channel test case. Figure 5 shows TI , root-mean-square of the x -velocity perturbations, $v'_{x,rms}$, turbulent length scale in the spanwise direction, L_y , and L_x plotted across a vertical slice through the domain at $x/H = -0.05$. The data was sampled for two flow residence times after starting the simulation with the turbulent inflow. The PIV measurements from UVASCF, also taken at $x/H = -0.05$, are shown. The computational results agree well with the PIV data, with both showing a TI ranging from 10 to 15% in the core flow. Turbulence intensity is more variable in the experimental data close to the wall, whereas in the simulation it increases steadily approaching the wall. In both the experiments and computations, the $v'_{x,rms}$ is approximately 45 m/s in the core flow, increasing slightly near the lower wall. The turbulent length scales in both streamwise and spanwise directions are both approximately 5 mm in the core flow. Similarity in L_x and L_y is expected, as the turbulence generated at the inflow is isotropic.

Figure 6 shows contours of T , velocity magnitude, $\|\mathbf{v}\|$, p , and Y_{CH2O} sampled two flow residence times after initializing the simulation. The velocity perturbations generated at the inflow are easily observed in the $\|\mathbf{v}\|$ plot. As in the constant-area channel test case, the high-frequency waves gradually diffuse as they propagate further into the domain. The pressure waves collide with and perturb the flame, causing the formation of turbulent structure along the flame surface. Despite the distortion to the flame surface,

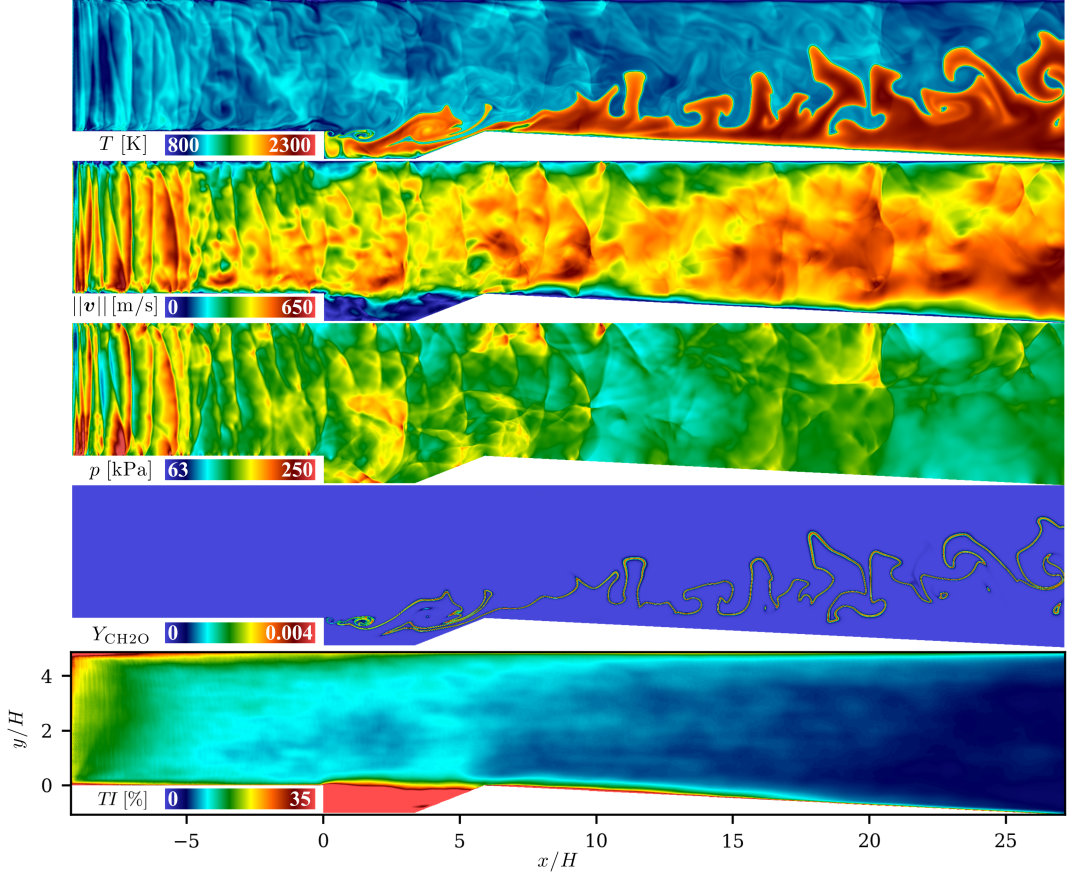


Figure 6: Contours of T , $||\mathbf{v}||$, p , $Y_{\text{CH}_2\text{O}}$, and TI for a cavity-stabilized flame with a turbulent inflow.

the flame remains anchored to the cavity lip indefinitely, consistent with experiments. Downstream of the cavity, in the expanding section of the combustor, the flame travels further into the core flow than in the laminar inflow case, resulting in higher fuel consumption over a shorter axial distance. Figure 6 also shows contours of time-averaged TI . The TI is $\sim 20\%$ in the core flow immediately downstream of the inflow boundary, gradually decaying to a value of 10% in the core flow just upstream of the cavity lip; this was the targeted value to match experimental conditions as shown in Fig. 5a. Recirculation in the cavity and near the walls causes TI to remain higher in these regions than in the core flow.

Figure 7 shows the time-averaged hydroxyl radical mass fraction, \bar{Y}_{OH} , for the laminar and turbulent inflow simulations and the mean OH PLIF signal from the experiment, all plotted over the same spatial domain. In both simulation and experiment, there is a decrease in OH concentration over the intersection of the cavity ramp and wall of the expanding section (at $y/H = 0$ and $x/H = 6.5$). The sharpness of the turning angle at this location results in local extinction of the flame. Reignition occurs immediately downstream. This local extinction event was captured in the simulations both with and without a turbulent inflow (see Figs. 2 and 6) and was also reported in the experiments [10]. The turbulent flame speed

correlation of Peters [11] was used to calculate the theoretical flame angle emanating from the cavity lip, shown as the solid white line in Fig. 7a. The experimentally measured flame angle, marked with the white dashed line, is slightly shallower than the theoretical prediction. The laminar inflow simulation did not reproduce the experimental flame angle, with all OH formation occurring much closer to the bottom wall than in the experiment. When the turbulent inflow was used the flame angle shows good agreement with the experiment indicating that the simulation accurately captures the time-averaged flame location. This result highlights the importance of freestream turbulence in promoting propagation of the flame into the incoming flow of reactants.

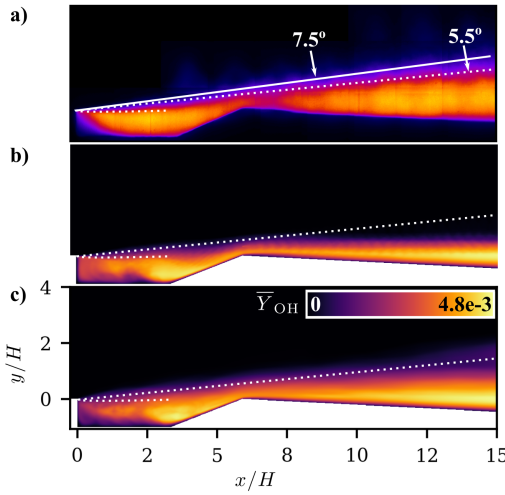


Figure 7: (a) Mean OH PLIF signal from UVASCF (b) \bar{Y}_{OH} from laminar inflow simulation (c) \bar{Y}_{OH} from turbulent inflow simulation.

4.4 Higher Order Solution

A subsequent simulation was performed using the same mesh as used in the previously described cases, but with third-order accurate $DG(p = 2)$ elements. In this configuration, the mesh resolution is $7.5 \mu\text{m}$ in the cavity shear layer, flame, and against the walls, growing to $55 \mu\text{m}$ in the core flow. This simulation was performed in order to assess differences in the level of detail captured in $DG(p = 1)$ and $DG(p = 2)$ solutions. The final time step of the $DG(p = 1)$ solution was used as the initial condition for the $DG(p = 2)$

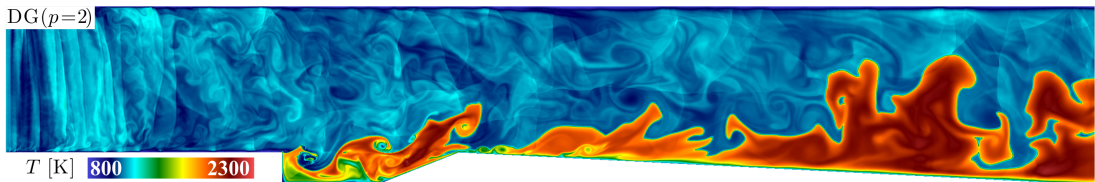


Figure 8: Temperature contours for $DG(p = 2)$ solution.

simulation. Figure 8 shows temperature contours for the $DG(p = 2)$ solution. In comparing Fig. 8 to the temperature contour plot in Fig. 6, it is apparent the the $DG(p = 2)$ solution resolves the acoustic waves generated by the turbulent inflow with more detail. However, the two simulations show similar structure along the flame surface and both resolve the local extinction of the flame as it propagates over the cavity ramp. In both cases, the flame remains anchored in the cavity and, downstream of the cavity, travels a comparable distance from the bottom wall into the core flow resulting in a consistent flame angle. The $DG(p = 1)$ solution is thus considered adequate for capturing the turbulence-flame interactions and resolving the physics of interest in this study.

5 Conclusions

This paper summarizes the numerical simulation of turbulent combustion in the University of Virginia Supersonic Combustion Facility using a synthetic turbulence inflow boundary condition to accurately and efficiently reproduce the turbulence intensity measured in experiments. Ramjet-mode operation of the facility at a combustor inflow Mach number of 0.6 was simulated, with a stagnation temperature of 1200 K corresponding to flight at Mach 5. The inflow was premixed ethylene-air with an equivalence ratio of 0.6 and a 19 species, 35 reaction step chemical mechanism was used to simulate ethylene-air combustion. Two cases were considered: (a) laminar inflow and (b) synthetic turbulence inflow. In both cases, a cavity-stabilized flame was achieved. The turbulent inflow boundary condition successfully reproduced the experimental measurements of the turbulent flow profile upstream of the combustor cavity. This allowed the accurate simulation of the fine-scale combustion in the cavity flameholder without incurring the computational expense of simulating the entire upstream domain.

Due to the high resolution in the simulations, local extinction of the flame as it propagated over the cavity ramp was observed, supporting the experimental observations. In the laminar inflow case, the flame angle was much shallower than that measured experimentally. The flame angle in the turbulent inflow case agreed with the experiment and with theory, indicating that the inflow turbulence has a significant effect on flame propagation into the core flow. The inflow turbulence promoted robust combustion as more of the incoming fuel was consumed in a shorter axial span than in the laminar inflow case.

Acknowledgments

The authors gratefully acknowledge the support of the Base Program at the Naval Research Laboratory.

References

- [1] A. Ben-Yakar, R. K. Hanson, Cavity flame-holders for ignition and flame stabilization in scramjets: an overview, *Journal of Propulsion and Power* 17 (4) (2001) 869–877.
- [2] C. C. Rasmussen, J. F. Driscoll, K.-Y. Hsu, J. M. Donbar, M. R. Gruber, C. D. Carter, Stability limits of cavity-stabilized flames in supersonic flow, *Proc. Combust. Inst.* 30 (2) (2005) 2825–2833.
- [3] D. J. Micka, J. F. Driscoll, Combustion characteristics of a dual-mode scramjet combustor with cavity flameholder, *Proc. Combust. Inst.* 32 (2) (2009) 2397–2404.
- [4] H. Wang, Z. Wang, M. Sun, N. Qin, Combustion characteristics in a supersonic combustor with hydrogen injection upstream of cavity flameholder, *Proc. Combust. Inst.* 34 (2) (2013) 2073–2082.
- [5] Q. Liu, D. Baccarella, W. Landsberg, A. Veeraragavan, T. Lee, Cavity flameholding in an optical axisymmetric scramjet in mach 4.5 flows, *Proc. Combust. Inst.* 37 (3) (2019) 3733–3740.
- [6] A. S. Potturi, J. R. Edwards, Large-eddy/Reynolds-averaged navier–stokes simulation of cavity-stabilized ethylene combustion, *Combust. Flame* 162 (4) (2015) 1176–1192.
- [7] R. D. Rockwell, C. P. Goyne, H. Chelliah, J. C. McDaniel, B. E. Rice, J. R. Edwards, L. M. Cantu, E. C. Gallo, A. D. Cutler, P. M. Danehy, Development of a premixed combustion capability for dual-mode scramjet experiments, *Journal of Propulsion and Power* 34 (2) (2018) 438–448.
- [8] P. M. Allison, K. Frederickson, J. W. Kirik, R. D. Rockwell, W. R. Lempert, J. A. Sutton, Investigation of supersonic combustion dynamics via 50 kHz CH* chemiluminescence imaging, *Proc. Combust. Inst.* 36 (2) (2017) 2849–2856.
- [9] C. M. Geipel, R. Rockwell, H. Chelliah, A. D. Cutler, C. Spelker, Z. Hashem, P. M. Danehy, in: 33rd AIAA Aerodynamic Measurement Technology and Ground Testing Conference, 2017.
- [10] C. M. Geipel, D. A. Lieber, V. G. Awate, R. D. Rockwell, H. K. Chelliah, C. P. Goyne, A. D. Cutler, in: AIAA Scitech 2019 Forum, 2019.
- [11] N. Peters, The turbulent burning velocity for large-scale and small-scale turbulence, *Journal of Fluid mechanics* 384 (1999) 107–132.
- [12] T. Nielsen, J. R. Edwards, H. K. Chelliah, D. A. Lieber, C. M. Geipel, C. P. Goyne, R. D. Rockwell, A. D. Cutler, in: AIAA Scitech 2019 Forum, 2019.
- [13] R. F. Johnson, A. D. Kercher, A conservative discontinuous Galerkin discretization for the total energy formulation of the reacting navier stokes equations (2019). [arXiv:1910.10544](https://arxiv.org/abs/1910.10544).
- [14] C. R. Wilke, A viscosity equation for gas mixtures, *J. Chem. Phys* 18 (1950) 517–519.
- [15] S. Mathur, P. K. Tondon, S. C. Saxena, Thermal conductivity of binary, ternary and quaternary mixtures of rare gases, *Molecular Physics* 12 (1967) 569–579.
- [16] R. J. Kee, J. A. Miller, G. H. Evans, G. Dixon-Lewis, A computational model of the structure and extinction of strained, opposed flow, premixed methane-air flames, *Proc. Combust. Inst.* 22 (1) (1989) 1479–1494.
- [17] S. Gottlieb, C. Shu, E. Tadmor, Strong stability-preserving high-order time discretization methods, *SIAM Review* 43 (1) (2001) 89–112.
- [18] G. Wanner, E. Hairer, *Solving ordinary differential equations II*, Springer Berlin Heidelberg, 1996.

- [19] G. Dong, B. Fan, J. Ye, Numerical investigation of ethylene flame bubble instability induced by shock waves, *Shock Waves* 17 (6) (2008) 409–419.
- [20] L. Davidson, Using isotropic synthetic fluctuations as inlet boundary conditions for unsteady simulations, *Advances and Applications in Fluid Mechanics* 1 (1) (2007) 1–35.